Redox Biology 50 (2022) 102256

Contents lists available at ScienceDirect

Redox Biology

journal homepage: www.elsevier.com/locate/redox

Reduction of lactoferrin aggravates neuronal ferroptosis after intracerebral hemorrhagic stroke in hyperglycemic mice

Zhongnan Xiao [a,b], Danmin Shen [a], Ting Lan [a], Chao Wei [c], Weihua Wu [a], Qingyu Sun [c], Zhaoli Luo [a], Wen Chen [c], Yurui Zhang [c], Liye Hu [a], Chenguang Zhang [a], Yamei Wang [a], Yabin Lu [a], Peipei Wang [c], Fei Yang [c,d], Qian Li [a,d,*]

[a] Department of Biochemistry and Molecular Biology, School of Basic Medical Sciences, Capital Medical University, Beijing, 100069, China
[b] Beijing Rehabilitation Hospital, Capital Medical University, Beijing, 100144, China
[c] Department of Neurobiology, School of Basic Medical Sciences, Capital Medical University, Beijing, 100069, China
[d] Advanced Innovation Center for Human Brain Protection, Beijing Key Laboratory of Neural Regeneration and Repair, Capital Medical University, Beijing, 100069, China

ARTICLE INFO

Keywords:
Intracerebral hemorrhagic stroke
Hyperglycemia
Ferroptosis
Neutrophil
PPARγ
Lactoferrin

ABSTRACT

Diabetic hyperglycemia aggravates the prognosis of intracerebral hemorrhagic stroke (ICH) in the clinic. In addition to hematoma expansion and increased inflammation, how diabetic hyperglycemia affects the outcomes of ICH is still unclear. We found that streptozotocin-induced diabetic hyperglycemia not only increased neutrophil infiltration, but also changed the gene expression profile of neutrophils, including lactoferrin (Ltf) encoding gene *Ltf*. Peroxisome proliferator-activated receptor γ (PPARγ) transcribed *Ltf* and the lack of neutrophilic Ltf transcription and secretion exacerbated neuronal ferroptosis by accumulating intraneuronal iron. Furthermore, the administration of recombinant Ltf protected against neuronal ferroptosis and improved neurobehavior in hyperglycemic ICH mice, and *vice versa*. These results indicate that supplementing Ltf or inhibiting neuronal ferroptosis are promising potential strategies to improve the acute outcomes of diabetic ICH in the clinic.

1. Introduction

Spontaneous intracerebral hemorrhagic stroke (ICH) is the most fatal stroke subtype worldwide [1]. More than one-third of ICH patients have diabetes or hypertension [2]. Diabetes increased the risk of mortality in patients and is an independent predictor of poor prognosis after ICH [3,4]. However, the molecular basis of diabetes exacerbating ICH injury is not fully understood. Previous studies by us and other labs have shown that red blood cells and their metabolites, such as Hemoglobin, Hemin, and iron, are transported into neurons and increase intracellular iron levels after ICH [5–7]. The enhanced iron-induced Fenton reaction leads to the accumulation of lipid reactive oxygen species (ROS) and leads to a form of neuronal death called ferroptosis [8], which is a regulated non-apoptotic cell death form [9]. Neuronal ferroptosis can be rescued by chelating iron (treating with Deferoxamine, DFO) [10], scavenging lipid ROS (treating with Ferrostatin-1, Fer-1) [11], or restoring neuronal glutathione peroxidases 4 (GPx4) activity [6] (treating with selenium) after ICH. Although the perihematomal neuronal ferroptosis is positively correlated with the severity of acute outcomes after ICH in healthy young mice [6,12–14], it is unclear whether diabetes exacerbates ICH outcomes by increasing neuronal ferroptosis and its underlying mechanisms.

In the clinic, the number of peripheral neutrophils in patients with ICH increases and serves as an independent predictor of poor prognosis [15]. In addition, preclinical studies have shown that peripheral circulating neutrophils and other immune cells are attracted by chemokines secreted by reactivated glial cells, and infiltrate to hematoma/perihematomal brain region, and affecte prognosis of ICH [16]. Neutrophils are the most abundant circulating white blood cells and play an important role in the innate immune response [17]. After ICH, neutrophils are the first cells to infiltrate the brain to release matrix metalloproteinases (MMPs), myeloperoxidase (MPO), neutrophil extracellular traps (NETs), and cytokines. Studies show that they aggravate blood-brain barrier (BBB) permeability, brain edema, hematoma growth, and inflammation [18–21]. However, little is known about

* Corresponding author. Department of Biochemistry and Molecular Biology, School of Basic Medical Sciences, Capital Medical University, Beijing, 100069, China.
E-mail address: qianli@ccmu.edu.cn (Q. Li).

https://doi.org/10.1016/j.redox.2022.102256
Received 21 December 2021; Received in revised form 27 January 2022; Accepted 28 January 2022
Available online 2 February 2022

Abbreviations

ICH	intracerebral hemorrhagic stroke
Ltf	lactoferrin
PPARγ	peroxisome proliferator-activated receptor γ
ROS	reactive oxygen species
DFO	deferoxamine
Fer-1	ferrostatin-1
GPx4	glutathione peroxidases 4
MMPs	matrix metalloproteinases
MPO	myeloperoxidase
NETs	neutrophil extracellular traps
BBB	blood-brain barrier
LfR	lactoferrin receptor
PFA	paraformaldehyde
CV	cresyl violet
MFI	fluorescence intensity
FJC	fluoro-Jade C
PI	propidium iodide
MDA	malondialdehyde
TBA	thiobarbituric acid
STZ	streptozotocin
HG	high glucose
NG	normal glucose
KEGG	Kyoto Encyclopedia of Genes and Genomes
ChIP	chromatin immunoprecipitation
ROSI	rosiglitazone
CM	conditioned media
COX-2	cyclooxygenase-2
GSH	glutathione
DMSO	dimethylsulfoxide

whether neutrophils crosstalk with damaged neurons and affect neuronal death.

Lactoferrin (Ltf) is an iron-binding glycoprotein and one of the most abundant proteins secreted by neutrophils [22]. The binding affinity of Ltf with Fe^{3+} is much higher than that with iron chelators, such as DFO [22–24]. It binds to the lactoferrin receptor (LfR) or other receptors (RAGE, TREM-1, CD14, and TLR2/4) [25] and is transported into the cells, and shapes functions of immune cells and neural stem cells [22]. Nevertheless, the effects of Ltf on neuronal ferroptosis and diabetic ICH remain unclear. The goal of this study was to determine the cause of aggravated ICH outcomes in diabetic mice and the underlying mechanism. The insights gained from this study will improve our understanding of innate immune regulation after diabetic ICH and will be crucial for advancing future translational and clinical research on neuroprotection.

2. Materials and methods

The ARRIVE and RIGOR guidelines [26] were followed (except that we do not use mice of both genders): animals that had a neurologic deficit score higher than 20 at 24 h after surgery were euthanized under deep anesthesia. Sample sizes were excluded the animals which were died or euthanized. All experiments were performed with three or more independent experiments. A power analysis based on our previous studies [6] and pilot data indicated that 8 mice/group would provide at least 80% power for detecting a 20% decrease in neurologic deficits at $\alpha = 0.05$ (2-sided). The website www.randomization.com was used for randomizing animals and cell cultures group. Treatment, data collection, and data analyses were blinded by using different investigators or by masking sample labels.

2.1. Animals

Adult male mice (WT, C57BL/6J mice, 6–12 weeks) which were obtained from Vital River (Beijing, China) were used for this study. All animals in this study were bred and housed under specific-pathogen-free conditions at Capital Medical University. Mice were housed in a regulated environment (22 ± 2 °C, 55 ± 5% humidity, and 12:12-h light:dark cycle with lights on at 8:00 a.m.) and received a standard diet. Food and water were accessible ad libitum. All animal experimental protocols were approved by the Institutional Animal Care and Use Committee of Beijing Capital Medical University.

2.2. Hyperglycemia ICH mouse models

Mice were randomly divided into two groups: Vehicle (Veh-injected group), hyperglycemia (STZ-injected group). After 12 h fasting (8:00–20:00) but not forbidden water, the STZ-injected group was induced by intraperitoneal injection with streptozotocin (STZ; S0130, Sigma-Aldrich) at 50 mg/kg body weight dissolved in 0.1 mmoL/L citrate buffer (pH 4.5) for 5 days before operation [27]. Mice in the vehicle group were injected with citrate buffer at the same volume as that administered to mice in the STZ-injected group. Blood glucose was measured by OneTouch Select Test Strips (Yuwell, Beijing, China) with the tail venous blood after 12 h fasting (8:00–20:00), and hyperglycemia was defined as fasting blood glucose >11.1 mmoL/L [28].

2.3. Intracerebral hemorrhage (ICH) mouse model

Mice were deeply anesthetized with isoflurane (mixture of 70% N_2O and 30% O_2; 3% induction, 1–2% maintenance) using an isoflurane vaporizer (RWD, Shenzhen, China) and aseptic experimental ICH surgery was induced in a stereotaxic frame (RWD, Shenzhen, China). A 0.6 mm burr hole was made in the left striatum, and a 26-gauge needle was inserted through the burr hole into the striatum (coordinates: 0.8 mm anterior, 3.0 mm ventral, and 2.0 mm lateral to the bregma). For the autologous blood injection model, 23 μL whole blood was injected into the left striatum at a rate of 0.5 μL/min. Blood removed from the tail venous was infused in two-time blocks (3.0 mm ventral: 6 μL followed by a 5 min pause and then 3.2 mm ventral 17 μL followed by a 10 min pause to prevent backflow). Sham-operated mice received the same head skin incision under isoflurane anesthesia and needle insertion. Body temperature was maintained during surgery with a rectal probe and a heating blanket. All efforts were made to minimize the number of animals used and ensure minimal suffering. Bodyweight, rectal temperature, and survival rate were recorded for each mouse from intraperitoneal injection of STZ to the end of the experiment.

2.4. Neurologic and motor function evaluations

Neurologic deficit score was assessed post-ICH at indicated time points, as previously reported [6]. An investigator blinded to the experimental cohort scored all mice on six neurologic tests, including body symmetry, gait, climbing, circling behavior, front limb symmetry, and compulsory circling. Each test was graded from 0 to 4. The forelimb placement test [6] was used to investigate the animals' responsiveness to vibrissae stimulation. Intact animals placed the contralateral forelimb quickly on the tabletop. The placing was quantified as the percentage of successful responses in 10 trials. The mouse was placed on the edge of a tabletop and the contralateral hind limb was pulled down [6]. The test was scored as follows: immediate pullback of limb = 0, delayed pullback = 1, inability to pull back = 2. The placing was quantified in 10

successful trials; trials were excluded when the animal attempted to turn around or walk away. Results are shown as a total score for each mouse. For the wire hanging test [29], the experimental apparatus was a stainless steel bar as described previously. Mice were placed on the bar midway between the supports and were observed for 30 s in each of four trials. The amount of time spent hanging was recorded and scored according to the following criteria: 0, fell off; 1, hung onto the bar with two forepaws; 2, hung onto the bar with an added attempt to climb onto the bar; 3, hung onto the bar with two forepaws and one or both hind paws; 4, hung onto the bar with all four paws and with tail wrapped around the bar; 5, escaped to one of the supports. The rotarod test was conducted to evaluate motor coordination and balance. Mice were trained for 3 days before ICH induction. At indicated time points after ICH, mice were placed on a rotarod apparatus. Each mouse was placed on the rod at a speed of 4 rotations per minute (rpm) which accelerated over the course of 300 s to 70 rpm. The duration of each mouse on the rod was recorded automatically. Each mouse was tested in four consecutive trials with an interval of 5 min. The results were calculated as the average of the last three trials.

2.5. Animal perfusion and tissue collection

Animals were anesthetized with chloral hydrate (0.5 g/kg, *i. p.*) and intracardially perfused with ice-cold PBS. The hematoma-affected striatum was stored at −80 °C before RNA isolation or protein extraction. For immunofluorescence and histochemistry analyses, 4% paraformaldehyde (PFA) was used for fixed following ice-cold PBS. The whole brain was dipped in 20%, 30%, 30% sucrose for 24 h respectively, then embedded with OCT for preparation of frozen sections.

2.6. Hemorrhagic injury analysis

Frozen coronal brain sections were stained with Cresyl violet (CV, stains neurons, C5042, Sigma-Aldrich) and Luxol fast blue (stains myelin, S3382, Sigma-Aldrich) at 16 rostral-caudal levels that were spaced 96 μm apart as reported previously [6]. Sections were digitized and analyzed with a 1 × objective and ImageJ software. The injury volume in cubic millimeters was computed by summation of the damaged areas multiplied by the interslice distance (96 μm).

2.7. Cell preparation and flow cytometry analysis

At 1 day following ICH, single-cell suspensions were prepared from fresh spleen or fresh brain tissue after cardiac perfusion and stained with fluorochrome-conjugated antibodies [30,31]. Briefly, ipsilateral hemispheres were sheared in DNase 1 (D8071, Solarbio), then brain tissue was incubated at 37 °C after adding papain working solution (Daspase II 1.2 U/mL + papain 1 mg/mL) (Daspase II 04942078001, Roche; papain P4762, Sigma-Aldrich). After centrifuged, the supernatant was discarded and re-suspended and filtered through a 70 μm cell strainer. Cells were centrifuged and re-suspended by the addition of 30% and 70% percoll (P8370, Solarbio), and then were washed by PBS. In each group, 1×10^6 cells were re-suspended in flow cytometry stationary buffer (00-4222-57, eBioscience) system. We distinguished live and dead cells by adding 7-aminoactinomycin D (7-AAD, 00-6993-50, eBioscience). The following antibodies were used for surface receptor detection: CD45-EFLUOR 455 (48-0451-82, eBioscience), CD11b-FITC (557396, BD), Ly6G-PE (551461, BD), CD3e-APC-EFLUOR 780 (47-0031-82, eBioscience). Unstained cells were used as a negative control to establish the flow cytometer voltage settings, and single-color positive controls were used to adjust compensation. Cells were washed and re-suspended in 0.01 M PBS and analyzed with a LSRFortessa SORP cytometer (BD Biosciences), then analyzed using FlowJo software V10. A single viable cell was obtained from all cells, and then the number of microglia, neutrophils, monocyte/macrophage, lymphocytes, and T cells was obtained according to the prescribed gate strategy: microglia ($7AAD^-CD11b^+CD45^{int}$) and infiltrating neutrophils ($7AAD^-CD11b^+Ly6G^+$), monocytes/macrophages ($7AAD^-CD11b^+CD45^{hi}$), lymphocytes ($7AAD^-CD45^+$), T cells ($7AAD^-CD3e^+CD45^+$).

2.8. RT^2 profiler PCR arrays of hemorrhagic brain tissue

Cytokines, chemokines, and growth factors in the brain were analyzed by RT^2 Profiler PCR Arrays according to the manufacturer's instructions on day 1 after ICH. Total RNA was extracted and purified from hemorrhagic brain tissue by standard Trizol extraction procedure. Then reverse transcription using the RT^2 first strand kit (330401, QIAGEN). Realtime-PCR was implemented according to the manufacturer's instructions of RT^2 profiler QC array-Plate D 1 array (330291, QIAGEN) on Biosystems models 7500 fast PCR instrument.

2.9. Intracerebroventricular (i.c.v.) injection of Ltf-siRNA

Lactoferrin siRNA (100 μm, sc-41372, Santa Cruz) is a pool of 3 target-specific 19–25 nt siRNAs designed to knock down gene expression. Intracerebroventricular administration was performed as previously described [32,33]. Briefly, the 26-gauge needle of a 5 μL Hamilton syringe was inserted into the left lateral ventricle through a cranial burr hole at the following coordinates (0.5 mm anterior and 0.9 mm left lateral to the bregma, 2.5 mm deep under dura). A microinfusion pump was used for intracerebroventricular injection at a rate of 0.1 μL/min. Control scramble siRNA (Scr-siRNA, sc-44238, Santa Cruz) or Ltf-siRNA were injected by 0.5 μL/mice. The needle was left in place for an additional 10 min at the end of infusion and was removed over a 3 min period. The surgical wound was sealed with Super Glue.

2.10. Immunofluorescence staining and analysis

At 1- and 3-days following ICH, the immunofluorescence was performed as previously prescribed [6]. Briefly, the frozen coronal slices were put into antigen repair solution and permeabilized with 1% Triton X-100 for 15min. Brain sections were blocked in 5% goat serum and incubated with anti-rabbit MPO (1:500, ab45977, Abcam), anti-rabbit NeuN (1:500, CST), anti-MDA [11E3] (1:200, ab243066, Abcam), anti-rabbit Iba1 (019–19741, Wako), anti-mouse Ly6G (551459, BD Biosciences), anti-mouse CD11b-FITC (Clone:M1/70, 1:200, 4306305, eBioscience), anti-rabbit Ltf (1:200, bs-5810R, Bioss) primary antibody at 4 °C overnight. Slices then incubated with goat anti-rabbit 594 (A11012, Invitrogen), goat anti-rabbit 488 (A11034, Invitrogen), goat anti-mouse 594 (A11005, Invitrogen), goat anti-mouse 488 (A11001, Invitrogen). Nuclei were visualized via a mounting medium containing DAPI (ZG1202, Vectarshield). Images were analyzed with a confocal microscope (TCS SP8 STED, Leica) and fluorescence microscope (ECLIPSE Ti–U, NIKON). Mean fluorescence intensity (MFI) was analyzed with ImageJ software.

2.11. Isolation of peripheral blood neutrophils for RNA-seq

Extraction of neutrophils from peripheral blood by percoll gradient centrifugation. Single-cell suspensions were prepared from pooled mouse blood 1 day after ICH induced by autologous blood injection or sham operations (Veh-injected or STZ-injected). Blood was centrifuged to remove serum, and dextran T-500 was added to precipitate red blood cells. Cells were suspended softly over 2.5 mL 78%, 2 mL 66%, and 2 mL 54% percoll layer reagent (from bottom to top) and centrifuged to separate peripheral blood neutrophils. Neutrophils between 78% and 66% were then washed twice with D-hanks buffer. Then 500 μL Trizol was added into neutrophils and store at −80 °C. Neutrophils were collected for RNA-seq analysis (provided by Beijing igeneCode Biotech Co., Ltd, Beijing, China). After filtering, the "clean reads" were aligned to the reference sequences with Bowtie2 (Version: v2.2.5) and then calculated gene expression level with RSEM (Version: v1.2.12).

2.12. Isolating neutrophils from blood and culturing in vitro

In the same protocol as mentioned above, the neutrophils were isolated from C57BL/6J mice and re-suspended with normal-glucose RPMI 1640 (normal glucose, NG) or high-glucose RPMI 1640 (high glucose, HG). The NG medium contained 11.1 mM D-glucose, while HG medium contained 25 mM D-glucose. After incubated at 37 °C for 12 h, the medium was collected and centrifuged. The supernatant was placed in a new 1.5 mL EP and labeled as normal-glucose conditional medium (NG-CM) and high-glucose conditional medium (HG-CM) respectively for co-culture with neurons. Trizol or RIPA were added into cells for Realtime RT-PCR and Western blot. Sorted neutrophils were analyzed by Wright-Giemsa staining according to the manufacturer's instructions.

2.13. ChIP assay

Primary neutrophils were obtained from peripheral blood of C57BL/6J mice used the same protocol as mentioned above. Then, 5×10^6 neutrophils were fixed by 1% formalin (prepared with PBS preheated at 37 °C). After washing and centrifugating, cells were lysed in lysis buffer (50 mM Tris-HCl, pH 8.0; 5 mM EDTA; 1% SDS) supplemented with protease inhibitors. Chromatin was sheared by sonication (VCX150, Sonics) for 4 times, centrifuged. Then, 80 μL dilution buffer (1% Triton X-100; 2 mM EDTA; 150 mM NaCl; 20 mM Tris-HCl, pH 8.0) into 20 μL supernatant as input group. Meanwhile, dilution buffer and 2 μL IgG (AP132, Thermo Scientific) or PPAR-γ rabbit polyclonal antibody (16643-1-AP, Proteintech) were added to supernatant. Immune complexes were rotated overnight and Protein A/G was added to the complexes for 2 h. The complexes were centrifugated, washed, and eluted. DNA was extracted by Animal tissue/cell Genomic DNA Extraction Kit (D1700, Solarbio). Gene-specific primers were designed using Oligo 7 and Primer 5 software and are listed in Supplemental Table 3. Three replicates for each group were performed. Input group used as the internal control and the relative expression enrichment of samples was calculated from ($2^{-\Delta\Delta CT}$).

2.14. Primary mouse cortical neuronal cultures

The mouse pups (postnatal 0–1) were sterilized with 75% ethanol (ANNJET, China) and then sacrificed. The brain was placed in pre-cooling Hanks' solution (H1045-500, Solarbio, China) with an ice bag pre-cooling to remove the meninges and blood vessels. Cortex was cut into 1 mm pieces in 0.5 mL DNase 1 (200 μg/mL, D8071, Solarbio), and digested by papain working solution (Daspase II 1.2 U/mL + papain 1 mg/mL; Daspase II 04942078001, Roche; papain P4762, Sigma-Aldrich). Supernatant cells were filtered through a 70 μm mesh filter (352350, Falcon), and seeded in a poly-D-lysine (P0899, Sigma-Aldrich)–coated plates. Cytarabine (PHR1787, Sigma-Aldrich) was added 24 h later to remove astrocytes, and the Neurobasal medium (containing B27 supplement) was changed every 3 days. The cortico-striatal cultures contained mostly neurons and <2% glia cells, as determined by immunofluorescence staining. Cells were used at 7–10 days.

2.15. Co-culture of neurons and neutrophils, drug administration, and siRNA transfection of neutrophils

A half-changing medium was used to co-culture the neurons: half medium was used the old neurobasal (NB) medium, the other half used NG, HG, NG-CM, HG-CM, or new neurobasal (25 mM D-glucose). In the half-changing medium, we adjusted the D-glucose concentration: NB, NG, and NG-CM group to 25 mM, HG and HG-CM group to 37.1 mM. For mouse primary cortical neurons, we added 50 μM Hemin, 50 μM DFO for 8, 16, 24 h for PI staining, lipid ROS examination.

To knock down the expression of Ltf in 2×10^6 neutrophils, scramble-siRNA (sc-44238, Santa cruz) or Ltf-siRNA (sc-41372, Santa cruz) were incubated with Lipofectamine 3000 Transfection Reagent (11668027, Invitrogen) according to the instructions of the manufacturer. After incubating for 6 h, the medium was changed, and culture was continued. After 48 h of transfection, the transfection efficiency was confirmed by Western blot.

Primary neutrophils were obtained from peripheral blood of C57BL/6J mice using Percoll. Purified neutrophils were incubated for 12 h in RPMI 1640 medium supplemented with 10% FBS and were respectively treated with the 10 μM PPAR-γ antagonist rosiglitazone (ROSI, S2556, Selleck) or the 10 μM PPAR-γ antagonist T0070907 (S2871, Selleck) diluted in dimethylsulfoxide (DMSO, D8418, Sigma-Aldrich). Then protein from neutrophils was used for Western blot.

2.16. Cell death assessments

For *in vivo* experiments, Fluoro-Jade C (FJC) staining was used to assess cell death at perihematomal region as reported previously [34,35]. Briefly, mice were anesthesia and cardiac perfusion, and coronal brain sections were stained with FJC (AG325, Millipore). Treated brain sections were observed and photographed under a fluorescence microscope (ECLIPSE Ti–U, NIKON) at an excitation wavelength of 450–490 nm.

To assess cell death *in vitro*, Propidium iodide (PI) was used. Briefly, 2×10^4 cells suspension was added to the 96-well plate. After the maturation, the cells were treated according to the experimental design, and the PI dye (P4170, Sigma-Aldrich) was added for 0.5 h, and the staining was observed under a microscope (ECLIPSE Ti–U, NIKON).

2.17. Lipid ROS measurement

After treating the cells according to the experimental design, the medium was discarded. Add diluted BODIPY 581/591C11 reagent (D3861, Invitrogen) to each well for 0.5 h. After the removal, the cells were washed and images were taken under a fluorescence microscope and the ratio of green fluorescence intensity to red fluorescence intensity was calculated using ImageJ.

2.18. MDA measurement

At day 1 following ICH, 10 mg brain tissue or 2×10^6 neurons were homogenized on ice in 300 μL of Malondialdehyde (MDA) Lysis Buffer (with 3 μL of BHT) (K739-100, Biovision), then centrifuged (13,000 g, 10 min). Add 600 μL of thiobarbituric acid (TBA) reagent into each vial containing standards and sample. Pipette 200 μL (from each 800 μL reaction mixture) into a 96-well microplate for analysis. Read the absorbance at 532 nm using a spectrophotometer (SpectraMax iD5, Molecular DEVICES).

2.19. Iron measurement

Briefly, 2×10^6 primary neurons were cultured to the 7th day in 6-well plates. According to the design, the drug was mixed into 1 mL neurobasal, and blank control well, positive control well, and solvent control well were set at the same time. After 4 h of treatment time, the cells were washed and papain was added into each well. The cell suspension was collected and centrifuged as well. Add 25 μL iron assay buffer into the cell precipitation and centrifuged to remove insoluble substances. Divide each sample into Fe^{2+} sample (10 μL/well) and Fe^{3+} sample (10 μL/well). The determination of intracellular Fe^{2+} and Fe^{3+} was measured using an Iron colorimetric assay kit according to the manufacturer's instructions. OD value was measured at 593 nm using a spectrophotometer (SpectraMax iD5, Molecular DEVICES). Taking the concentration as the abscissa and the OD value as the ordinate, the standard curve was made, and Sa was obtained from the standard curve. Sv was the sample volume added into 96 well plates. For extracellular iron in the medium, 100 μL medium was used as Sv. The formula for

calculating the concentration of Fe^{2+}, total iron, and Fe^{3+} in the sample: C = Sa/Sv (nmoL/μL or mM).

2.20. Ltf administration in vivo and in vitro

In STZ-injected mice, human recombinant-Ltf (rLtf, L4040, Sigma-Aldrich, 0.05–0.10% iron saturated) was injected *i. p.* at 1 mg/kg, 4 mg/kg, 10 mg/kg in sterilized water, pH 7.2 (or sterilized water alone for vehicle control), immediately after ICH. For cell culture study, the rLtf (10 μg/mL, 100 μg/mL, 200 μg/mL) was added to the culture medium at the same time as treatment by Hemin.

2.21. Realtime RT-PCR analysis

Total mRNA was extracted from cells or the left striatum brain tissues (1 or 3 days after ICH) using Trizol reagent (15596026, Life technologies). The cDNA was synthesized using a reverse transcription kit (R223-01, Vazyme), and Realtime RT-PCR experiments (Applied Biosystem) were performed according to the instructions. The relative expression amount of each pair of samples was calculated from ($2^{-\Delta\Delta CT}$). The primers used were shown in Table S1.

2.22. Western blot

Total protein from cells or tissues was extracted with RIPA (C1053, Applygen). Total protein was quantified by BCA protein assay (23228, Thermo Scientific). All samples were electrophoresed on 10% SDS-PAGE gels before being transferred to a polyvinylidene fluoride membrane (Millipore). Membranes were blocked in 5% skim milk and then incubated with primary antibody overnight at 4 °C. The primary antibodies used in this study were as follows: Ltf (1:250, bs-5810R, Bioss), α-tubulin (B1052, Biodragon, Beijing), β-actin (sc-47778, Santa Cruz). After being treated with the secondary antibodies for 1 h, the protein bands were observed with ECL chemiluminescence solution. The relative intensity of protein signals was normalized to the corresponding loading control intensity and quantified by densitometric analysis with ImageJ software (https://imagej.nih.gov/ij/).

2.23. Cell counts

The cell counts were performed on days 1, 3 after ICH. For quantification of the MPO^+ cells, $Ly6G^+Ltf^+$ cells and FJC^+ cells in the perihematomal area consecutive slices were made, and 4 random fields around hematoma on six brain sections at 3 slides (1.2, 0.2, −0.8 mm anterior or posterior to bregma) 24 high-power images (40 × agnifification) per animal were used for cell counts. The average immunofluorescence intensity (MFI) was quantified using 4 random fields around hematoma on 2 slides (0.8, −0.8 mm anterior or posterior to bregma), and a total of 16 high-power images (40 × agnifification) per animal were used. For quantification of PI^+ cells , three fields (20 × agnifification) were counted and averaged. Cell counts were performed by two researchers in a blinded manner. All measurements were repeated three times, and the mean value was used.

2.24. Statistical analysis

Data are presented as mean ± SD, dot plot, or box-and-whisker plots (95% confidence intervals). Mean value is the average data obtained from all animals (*in vivo* experiments) or from three or more independent experiments (*in vitro* experiments). All data analysis was performed using GraphPad Prism 7.0 Software and was conducted by an experimenter blinded to the experimental conditions. We made 2-group comparisons with unpaired two-tailed Student's *t*-test. Compare the mean values of multiple groups, One-way ANOVA followed by Tukey's multiple comparisons test, Two-way ANOVA followed by Sidak's multiple comparisons test, or Tukey's multiple comparisons tests were used to determine where those differences occurred. The criterion for statistical significance was $p < 0.05$.

3. Results

3.1. Diabetic hyperglycemia exacerbates neuronal ferroptosis and aggravates acute outcomes after ICH

To investigate whether diabetic hyperglycemia aggravated acute outcomes after ICH by exacerbating neuronal ferroptosis, we intraperitoneal injected streptozotocin (STZ) or vehicle to C57BL/6 mouse for 5 days and intracranially injected autologous blood into the striatum (Fig. S1A). STZ injection markedly elevated blood glucose levels (Fig. S1B), slowed-down body weight increase (Fig. S1C), and affected rectal temperature (Fig. S1D).

Perihematomal neuronal ferroptosis is the major neuronal death post ICH [6,11,36–38], and the severity of ferroptotic neuronal loss positively correlates with neurobehavior deficits [6,37]. We accessed the number of degenerating neurons by Fluoro-Jade C (FJC) staining after ICH. STZ-injected ICH mice exhibited an increased profile of FJC^+ cells in the perihematomal region at both time points (Fig. 1A and B). Of note, no differences of FJC^+ cells were noticed between vehicle- and STZ-injection in sham-operated animals, indicating that hyperglycemia could be insufficient to induce neuronal death *in vivo*. Malondialdehyde (MDA) is an end-product of polyunsaturated fatty acid peroxidation and the accumulation of MDA is a hallmark of ferroptosis [6,39,40]. We immunostained MDA and NeuN (a neuronal marker) in the perihematomal region. The majority of $NeuN^+$ cells were MDA^+, suggesting that neuronal ferroptosis is a major form of cell death post ICH (Fig. 1C). Additionally, MDA fluorescent intensity was increased in hyperglycemic ICH mice compared with that in normoglycemic ICH mice (Fig. 1D). We verified this result by using a commercial MDA quantification kit (Fig. S1E). Cresyl violet and Luxol fast blue double staining showed that the lesion volume was also increased in hyperglycemic ICH mice (Fig. 1E and F). Since neuronal death contributes to neurologic deficits and motor dysfunction greatly, we performed the neurologic deficit score, forelimb placing test, hindlimb placing test, and wire hanging test up to 7 days after ICH (Fig. 1G–J). As expected, compared with normoglycemic ICH mice, hyperglycemic ICH mice exhibited severer neurologic deficits, decreased muscle tension, and aggravated motor dysfunction. These results suggest that hyperglycemic mice exacerbated neuronal ferroptosis and acute outcomes after ICH *in vivo*.

We next cultured mouse primary cortical neurons. Hemin was used to mimic ICH [41], and different concentrations of glucose incubation was used to mimic diabetic hyperglycemia and normoglycemia *in vitro*. The glucose concentration in the striata of hyperglycemic mice is about 1.5 times higher than that of normoglycemic mice (Fig. S2A). Basing on the data we collected and reports in the literatures [42,43], we considered 37.1 mM as high glucose (HG) and 25 mM as normal glucose (NG) for neuronal cultures *in vitro* (Fig. S2B). Next, we assessed neuronal death with Propidium Iodide (PI) staining. We found that Hemin induced neuronal death, but the percentage of cell death in high and normal glucose media-cultured neurons was similar (Figs. S2C and D). This result indicates that hyperglycemia is not sufficient to induce or aggravate neuronal ferroptosis after ICH *in vitro* and *in vivo*. Of note, we did not notice any differences in the profiles of FJC^+ cells nor MDA^+NeuN^+ cells between vehicle- and STZ-injection in sham-operated animals *in vivo* as well (Fig. 1A–D).

3.2. Diabetic hyperglycemic increases neutrophil infiltration post ICH

Since resident microglia and infiltrated peripheral immune cells (such as monocytes/macrophages, neutrophils, and lymphocytes) contribute to neurobehavior deficits after ICH [18,19,44], we assessed the number and percentage of immune cells in the perihematomal region after ICH (Fig. 2A). The ratio and absolute cell count of infiltrated

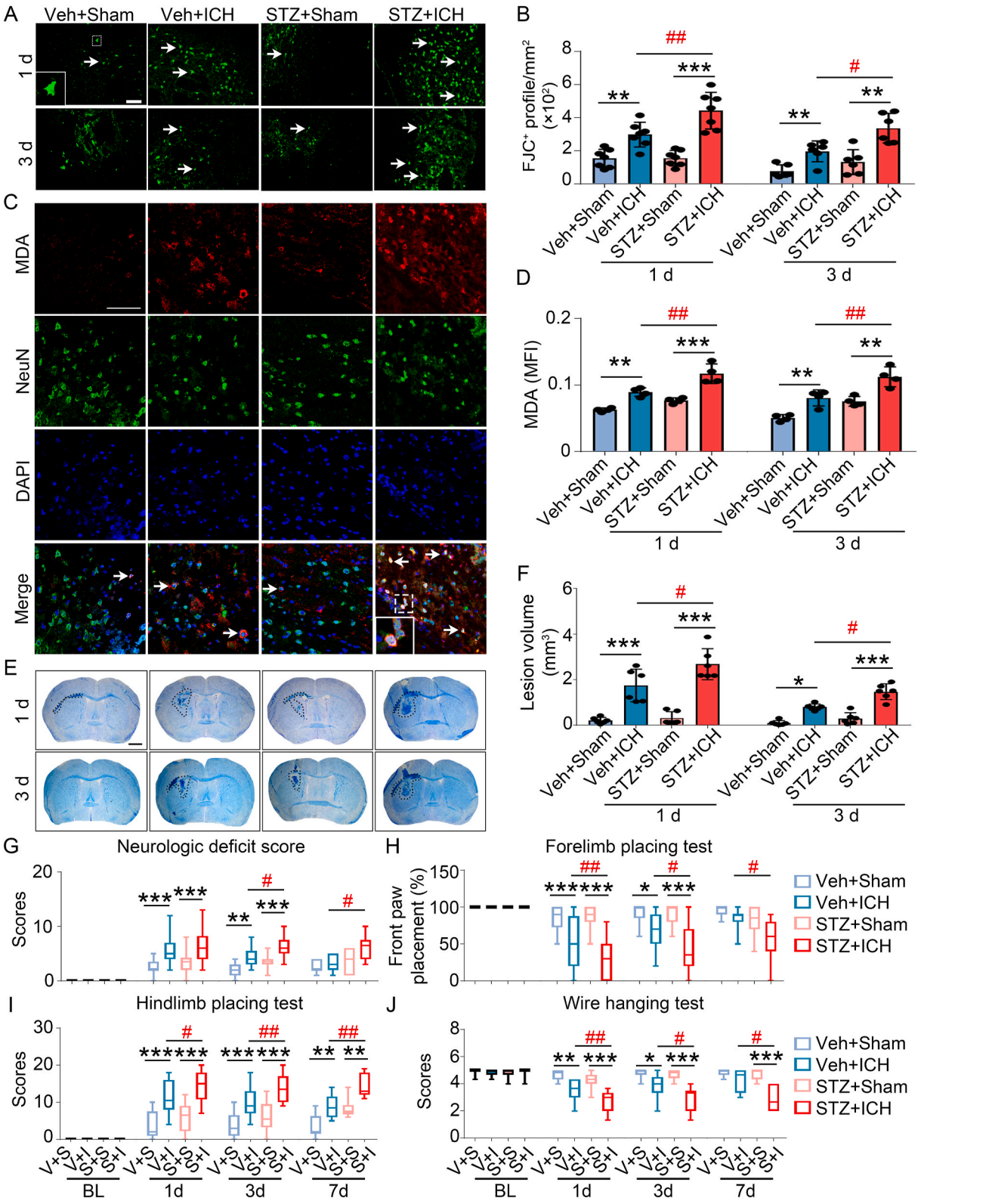

Fig. 1. Hyperglycemia increases neuronal ferroptosis and aggravates acute outcomes after ICH. (A–F) Brain slices obtained at day 1 and 3 post ICH were stained with FJC (A, B), MDA and NeuN (C, D), or CV/Luxol fast blue (E, F). **(A, B)** FJC staining represents degenerating neurons. The high power image of FJC^+ cell was shown in the white box. White arrows indicate FJC^+ cells. **(C, D)** Immunofluorescence of MDA and NeuN was performed. Representative images were shown at 1-day post-ICH. The high-power image of a $NeuN^+MDA^+$ cell was shown in the white box. White arrows indicate double positive cells. The mean fluorescence intensity of MDA was quantified (D). **(E, F)** Lesion volume (black dotted bordered) was calculated by CV/Luxol fast blue staining. **(G–J)** Acute outcomes were examined up to 7 days after ICH. (B, D, F-J) Two-way ANOVA followed Tukey's multiple comparisons test. $*p < 0.05$, $**p < 0.01$, $***p < 0.001$ vs corresponding Sham; $\#p < 0.05$, $\#\#p < 0.01$ vs Veh + ICH. Each group contained 6–7 (B), 6 (F), 4 (D), and 10–30 (G–J) animals. Scale bar: (A) 50 μm, (C) 75 μm, (E) 1 mm. Each experiment was repeated at least 3 times independently. (For interpretation of the references to color in this figure legend, the reader is referred to the Web version of this article.)

neutrophils (7AAD$^-$CD11b$^+$Ly6G$^+$) were markedly increased in hyperglycemic ICH mice in ipsilateral brain tissue at day 1 post-ICH (Fig. 2B, C, and Fig. S3A). No difference of cell count nor ratio was detected in resident microglia (7AAD$^-$CD11b$^+$CD45^{int}), monocytes/macrophages (7AAD$^-$CD11b$^+$CD45^{hi}), lymphocytes (7AAD$^-$CD45$^+$) or T cells (7AAD$^-$CD3e$^+$CD45$^+$) between normoglycemia and hyperglycemic ICH mice (Fig. 2D–G, S3B-E). Results gained from flow cytometry were further confirmed with immunostaining by using a constituent neutrophilic granules marker myeloperoxidase (MPO) (Fig. 2H and I) [45].

Neutrophil infiltration after ICH is usually regulated by certain chemokines/cytokines released by reactivated glial cells in the perihematomal region [46]. We next assessed the levels of

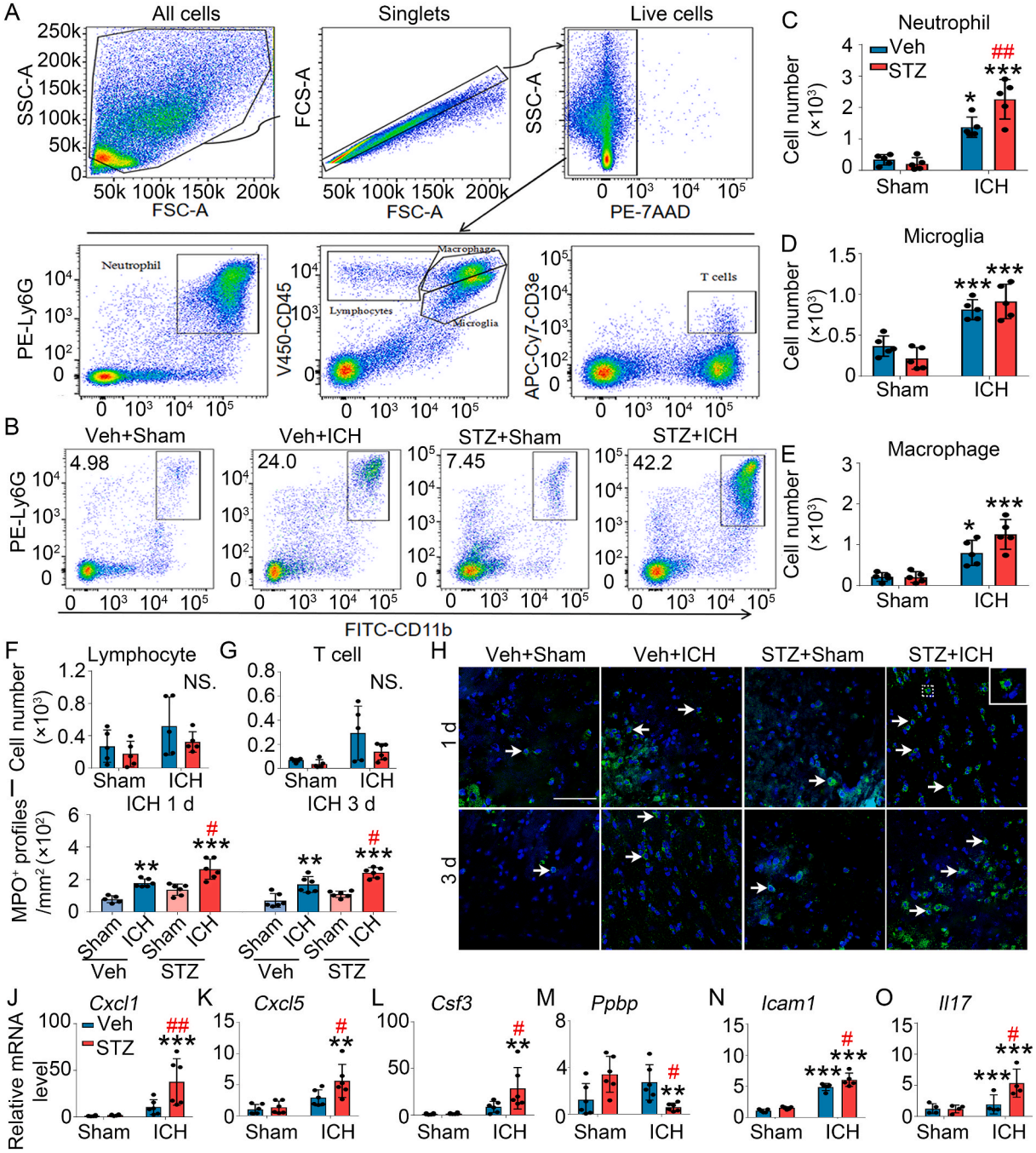

Fig. 2. Neutrophilic infiltration increases in the perihematomal region in hyperglycemic ICH mice. (A–G) Ipsilateral striata were dissected and flow cytometry was performed at 1-day post ICH. (A) Gating strategy of identifying resident microglia (7AAD$^-$CD11b$^+$CD45^{int}), neutrophils (7AAD$^-$CD11b$^+$Ly6G$^+$), monocytes/macrophages (7AAD$^-$CD11b$^+$CD45^{hi}), lymphocytes (7AAD$^-$CD45$^+$), and T cells (7AAD$^-$CD3e$^+$CD45$^+$). (B) Representative plots of the infiltrating neutrophils in different group are shown. Quantifications of the percentage of neutrophil (C), resident microglia (D), monocyte/macrophage (E), lymphocyte (F) and T cell counts (G) are shown. **(H, I)** Immunostaining using antibodies of MPO was performed at 1 and 3 days after ICH. White arrows indicate MPO$^+$ cells. The representative images (H) and quantifications (I) are shown. **(J–O)** The mRNA was extracted from ipsilateral striata of each group at day 1 after ICH, and real-time RT-PCR was performed to verify the gene expression of cytokines/chemokines. *GAPDH* was served as the internal control. (C-G, J-O) Two-way ANOVA followed by Sidak's multiple comparisons test. (I) Two-way ANOVA followed Tukey's multiple comparisons test. $^*p < 0.05$, $^{**}p < 0.01$, $^{***}p < 0.001$ vs corresponding Sham. $\#p < 0.05$, $\#\#p < 0.01$ vs Veh + ICH; NS., not significant. Each group contained 5 (C–G), 6 (I), 6 (J–M) and 4 (N, O) animals. Scale bar: (H) 75 μm. Each experiment was repeated at least 3 times independently.

chemokines/cytokines in ipsilateral brain tissue by RT^2 Profiler PCR array at 1 day after ICH (Fig. S3F). The mRNA expression level of chemokines that mediating neutrophil infiltration (such as *Cxcl1*, *Cxcl5*, and *Csf3* [47,48]) increased in hyperglycemic ICH mice compared with that in normoglycemic ICH mice, but not the chemokines mediating monocyte/macrophage infiltration (such as *Il2* and *CSF2* [49,50]) or T cell infiltration (such as *Ccl2* and *Ccl3* [51,52]) (Figs. S3F and G). We further verified the gene expression of chemokines mediating neutrophil infiltration using Realtime RT-PCR, and found that except *Ppbp*, the expression of *Cxcl1*, *Cxcl5*, *Csf3*, *Icam1*, and *Il17* were statistically increased in hyperglycemic ICH mouse brain (Fig. 2J-O).

3.3. Hyperglycemic mice exhibit decreased neutrophilic lactoferrin in peripheral blood and perihematomal region after ICH

To assess the changes in the gene expression profile of neutrophils affected by hyperglycemia and ICH, we collected neutrophils from peripheral circulation and performed RNA-seq experiment on day 1 after ICH. Gene expression profile was affected by both hyperglycemia and ICH greatly (Fig. S4A). Kyoto Encyclopedia of Genes and Genomes (KEGG) pathway analysis showed that plenty of vital pathways changed in peripheral neutrophils (Figs. S4B and C). We verified the results of RNA-seq by using Realtime RT-PCR (Fig. 3A). Between normoglycemic ICH mice and hyperglycemic ICH mice, 142 genes were upregulated, and 73 genes were downregulated (Fig. 3B). Among those genes, we noticed that *Ltf*, the gene that encodes iron-binding protein lactoferrin (Ltf) was slightly increased in normoglycemic ICH mice and markedly decreased in peripheral neutrophils in hyperglycemic ICH mice (Fig. 3B and C). The protein level of neutrophilic Ltf was significantly decreased in the perihematomal region in STZ-injected ICH mice (Fig. 3D and E). In addition, the expression of neutrophilic Ltf also significantly decreased in the perihematomal region in STZ-injected ICH mice assessed by immunostaining (Fig. 3F and G).

Dysregulation of peroxisome proliferator-activated receptor γ (PPAR-γ) signaling pathway contributes to type 2 diabetes, whether activating the PPAR-γ signaling pathway is beneficial to the prognosis of ICH associated with type 1 diabetes is still unclear [53,54]. We isolated peripheral neutrophils from naïve mice and performed chromatin immunoprecipitation (ChIP) assays using PPAR-γ antibodies. As shown in Fig. 3H, PPAR-γ directly bound to *Ltf* gene. ChIP followed by Realtime PCR also confirmed this result (Fig. 3I). In addition, the protein level of Ltf was increased by treating with PPAR-γ agonist rosiglitazone (ROSI) and decreased by treating with PPAR-γ antagonist T0070907 in peripheral neutrophils (Fig. 3J and K).

3.4. High glucose-reduced neutrophilic Ltf aggravates neuronal ferroptosis by affecting intracellular iron levels in vitro

We next incubated peripheral neutrophils in HG or NG *in vitro*. HG incubation markedly decreased neutrophilic *Ltf* mRNA level, intracellular Ltf protein level, and secreted Ltf protein level in conditioned media (CM) (Fig. 4A–C). We further collected CM from HG- or NG-cultured neutrophils and incubated them with mouse primary cortical neurons to assess the neuronal death with PI staining (Fig. 4D). Hemin induced neuronal death, further addition of neutrophilic CM collected from HG (HG-CM) enhanced neuronal death significantly (Fig. 4E and F). To determine whether HG-CM aggravated Hemin-induced neuronal death was due to lack of neutrophilic Ltf, we supplemented recombinant Ltf (rLtf) to HG-CM and found that the addition of 100 μg/mL rLtf to neutrophilic HG-CM was efficiently rescued neuronal death, as did in the DFO addition group (Fig. 4G, H and Figs. S5A and B). In addition, we transfected neutrophils with *Ltf*-siRNA or scramble-siRNA (Figs. S5C and D), collected CM, and incubated it with mouse primary neurons. Neuronal death was increased when co-culturing with CM collected from *Ltf*-siRNA neutrophils (Fig. 4I and J). Furthermore, the addition of Ltf neutralizing antibody to neutrophilic NG-CM also enhanced neuronal death compared with that in control cells (Fig. 4K and L).

Intracellular iron overload is the main cause of neuronal ferroptosis post-ICH [6,55]. To investigate whether Ltf rescued Hemin-induced ferroptosis and its underlying mechanism, we detected iron concentrations in indicated treatment groups in primary neurons. The addition of rLtf successfully decreased intracellular Fe^{2+} (Fig. 5A) and Fe^{3+} (Fig. 5B) concentrations as did DFO in both Hemin- and $FeCl_2$-treated neurons. Interestingly, rLtf did not decrease extracellular Fe^{2+} (Fig. 5C) and Fe^{3+} (Fig. 5D) concentrations in both Hemin- and $FeCl_2$-treated neurons, indicating that Ltf doesn't bind to iron in the media and doesn't bring extra iron into neurons.

The increase of lipid ROS, MDA content, and cyclooxygenase-2 (COX-2) coding gene *Ptgs2* overexpression are hallmarks of ferroptosis. Treating neurons with rLtf significantly decreased lipid ROS (Fig. 5E and F), MDA accumulation (Fig. 5G), and *Ptgs2* mRNA level (Fig. 5H) compared with Hemin-treated cells. These data further confirmed that Ltf rescued neuronal ferroptosis.

3.5. Administration of rLtf rescues neuronal ferroptosis and protects hyperglycemic mouse brain after ICH in vivo

We intracerebroventricularly injected *Ltf*-siRNA or scramble-siRNA into normoglycemic ICH mice. Western blots and immunostaining results showed that Ltf protein level was significantly downregulated after *Ltf*-siRNA infusion, especially in Ly6G$^+$ infiltrating neutrophils (Figs. S6A–D). We immunostained brain section with MDA and NeuN, and knocking down of intracerebral *Ltf* significantly increased perihematomal neuronal MDA accumulation (Fig. 6A and B). The profile of FJC$^+$ degenerating neurons (Fig. 6C and D) and lesion volume (Fig. 6E and F) were also increased after *Ltf*-siRNA infusion compared with that in the scramble-siRNA group. More importantly, normoglycemic ICH mice infused with *Ltf*-siRNA displayed significantly greater neurobehavioral deficits, lower forelimb placing score, higher hindlimb placing score, and decreased latency in wire hanging test and Rotarod test (Fig. 6G).

Furthermore, to detect whether rLtf supplementation had a therapeutic effect in hyperglycemic ICH mice, we intraperitoneally injected rLtf (1, 4, or 10 mg/kg) into hyperglycemic mice challenged with ICH and measured neurologic deficits at different time points. Among the different dosages, 4 mg/kg of rLtf provided the most robust behavior improvement in hyperglycemic ICH mice (Fig. S6E). We found that administration of rLtf (4 mg/kg) markedly decreased neuronal MDA accumulation (Fig. 6H and I), the profile of FJC$^+$ degenerative neurons (Fig. 6J and K), and lesion volume (Fig. 6L and M) in hyperglycemic ICH mice. Neurologic deficits and motor dysfunction were also efficiently rescued by administering rLtf compared with that in the vehicle group in hyperglycemic ICH mice (Fig. 6N).

4. Discussion

Spontaneous intracerebral hemorrhage (ICH) is the most lethal type of stroke. Currently, most preclinical studies have focused on ICH using young and healthy mice. However, clinically, between 2% and 27% of ICH patients aged 35–74 years have chronic underlying conditions, such as hypertension and diabetes [56]. Among those, diabetes is considered to be an independent predictor of poor outcomes after ICH and increases mortality in patients with ICH [56]. Diabetic hyperglycemia increases blood-brain barrier (BBB) permeability [57,58] and subsequently expands hematoma volume [59–61], increases inflammation [62,63], and aggravates white matter damage [64]. However, little is known about how diabetic hyperglycemia affects the process of neuronal death and nerve repair after ICH, which is the most direct cause of neurobehavior and motor dysfunction.

In the current study, we verified that diabetic hyperglycemia exacerbated neurologic deficits and motor dysfunction after ICH in the acute stage, which is consistent with clinical observations [65]. We also

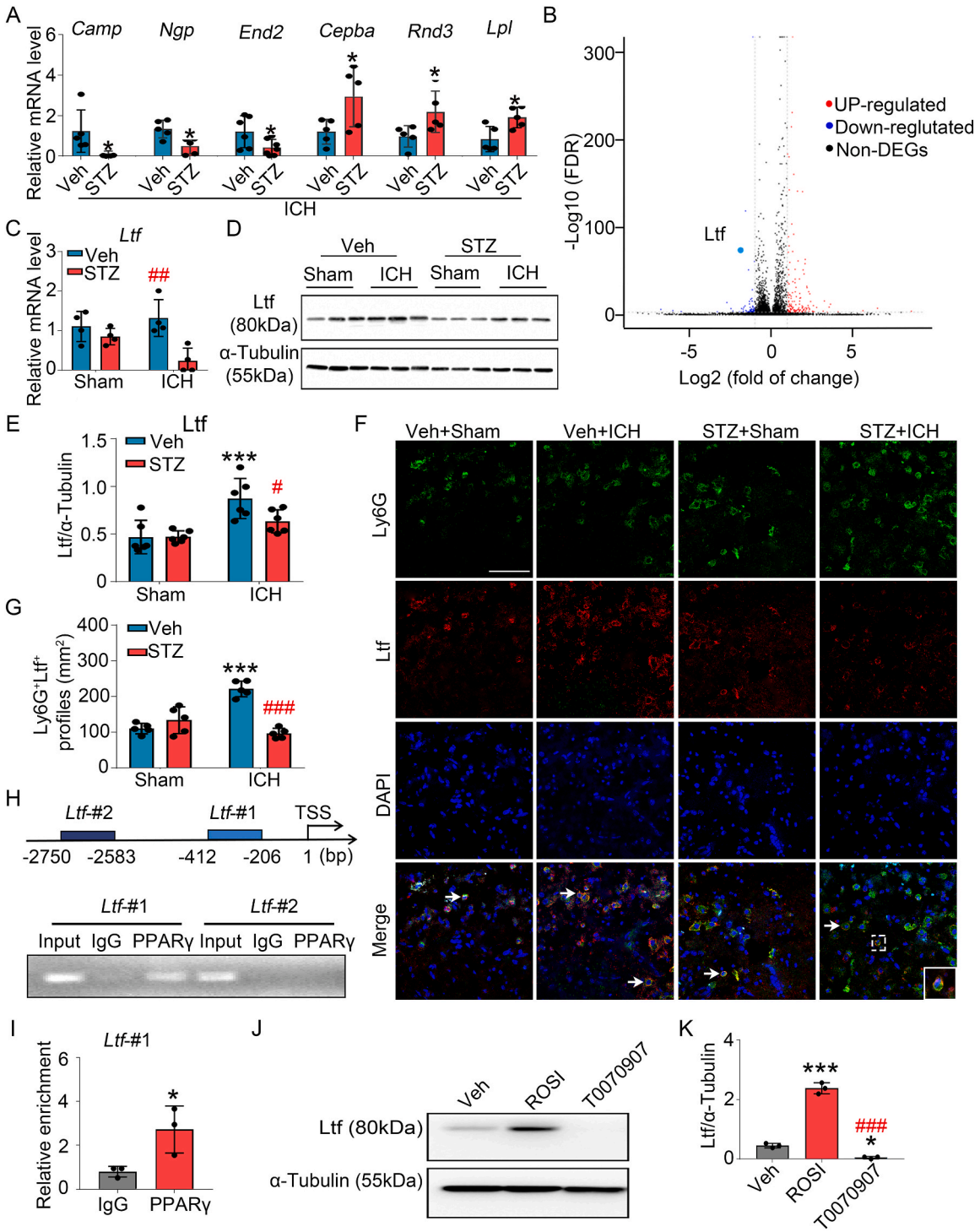

Fig. 3. Neutrophilic *Ltf* is downregulated in hyperglycemic ICH mice. (A) RNA-seq experiment was performed using peripheral neutrophils obtained at 1 day after ICH from each group. **(B)** A volcano plot showed the upregulated (red) and downregulated (blue) genes between STZ-injected mice and Vehicle-injected mice detected using RNA-seq. *Ltf* was showed by the blue spot. **(C)** Real-time RT-PCR was performed using peripheral neutrophils at 1 day after ICH. *GAPDH* was served as the internal control. **(D, E)** The protein level of Ltf was detected from ipsilateral striata using Western blot. The representative images (D) and quantifications (E) are shown. α-Tubulin was served as the internal control. **(F, G)** Immunostaining was performed using Ly6G and Ltf antibodies at 1-day post ICH. White arrows indicate double positive cells. The representative images (F) and quantifications (G) are shown. The high-power image of $Ly6G^{+}Ltf^{+}$ cell is shown in the white box. **(H, I)** Mouse primary neutrophils were cultured, and ChIP assays was performed using PPAR-γ antibodies. The location of two pairs of primers is shown. Agarose gel electrophoresis (H) and real-time PCR (I) were used following ChIP assays. **(J, K)** Mouse primary neutrophils were treated as indicated for 12 h. The expression of Ltf were measured by Western blot. α-Tubulin was served as the internal control. (A, I) Student's *t*-test followed by Welch's correction. (C, E, G) Two-way ANOVA followed by Sidak's multiple comparisons test. (K) One-way ANOVA followed Tukey's multiple comparisons test. $*p < 0.05$, $***p < 0.001$ vs corresponding Veh (A, K), corresponding Sham (C, E, J), or IgG (I); $\#p < 0.05$, $\#\#p < 0.01$, $\#\#\#p < 0.001$ vs Veh + ICH (C, E, G) or ROSI (K). Each group contained 3 (B), 5 (A, G), 4 (C), 6 (E) animals and 3 (I, K) independent experiments. Scale bar: (F) 75 μm. (For interpretation of the references to color in this figure legend, the reader is referred to the Web version of this article.)

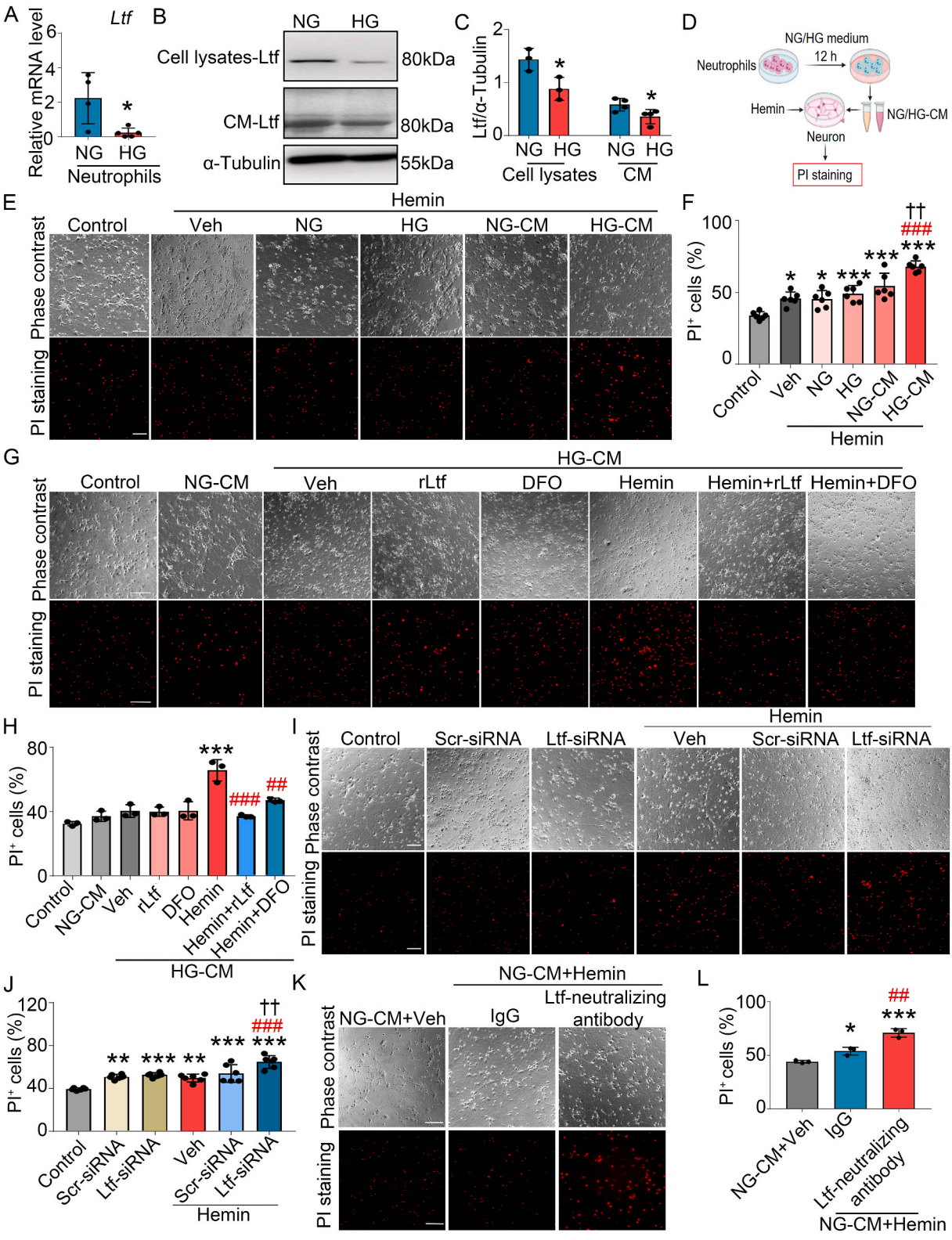

Fig. 4. High glucose reduced neutrophilic *Ltf* aggravates neuronal ferroptosis *in vitro*. Mouse primary peripheral neutrophils were extracted and cultured in normal-glucose (NG), high-glucose (HG) medium, or transfected with siRNA before use. **(A)** The mRNA level of *Ltf* was detected by real-time RT-PCR. *GAPDH* was served as the internal control. **(B, C)** The protein levels of Ltf in neutrophils (cell lysates-Ltf) and in conditional medium (CM-Ltf) were detect using Western blot. The representative images (B) and quantifications (C) are shown. α-Tubulin was served as the internal control. **(D)** Schematic of co-culturing mouse primary neurons and neutrophils. **(E–L)** Primary mouse neurons were treated as indicated for 8 h before performing PI staining. The representative images (E, G, I, K) and quantifications (F, H, J, L) are shown. (A, C) Student's *t*-test followed by Welch's correction. (F, H, J, L) One-way ANOVA followed Tukey's multiple comparisons test. $^{*}p < 0.05$, $^{**}p < 0.01$, $^{***}p < 0.001$ vs NG (A, C), Control (F, H, J), or NG-CM + Veh (L); $\#\#p < 0.01$, $\#\#\#p < 0.001$ vs Hemin + Veh (F, J), HG-CM + Hemin (H), or NG-CM + Hemin + IgG (L); $\dagger\dagger p < 0.01$ vs Hemin + NG-CM (F) or Hemin + Scr-siRNA (J). Each experiment was repeated 3–4 (C), 4 (A), 6 (F, J), or 3 (H, L) times independently. Scale bar: (E, G, I, K) 100 μm.

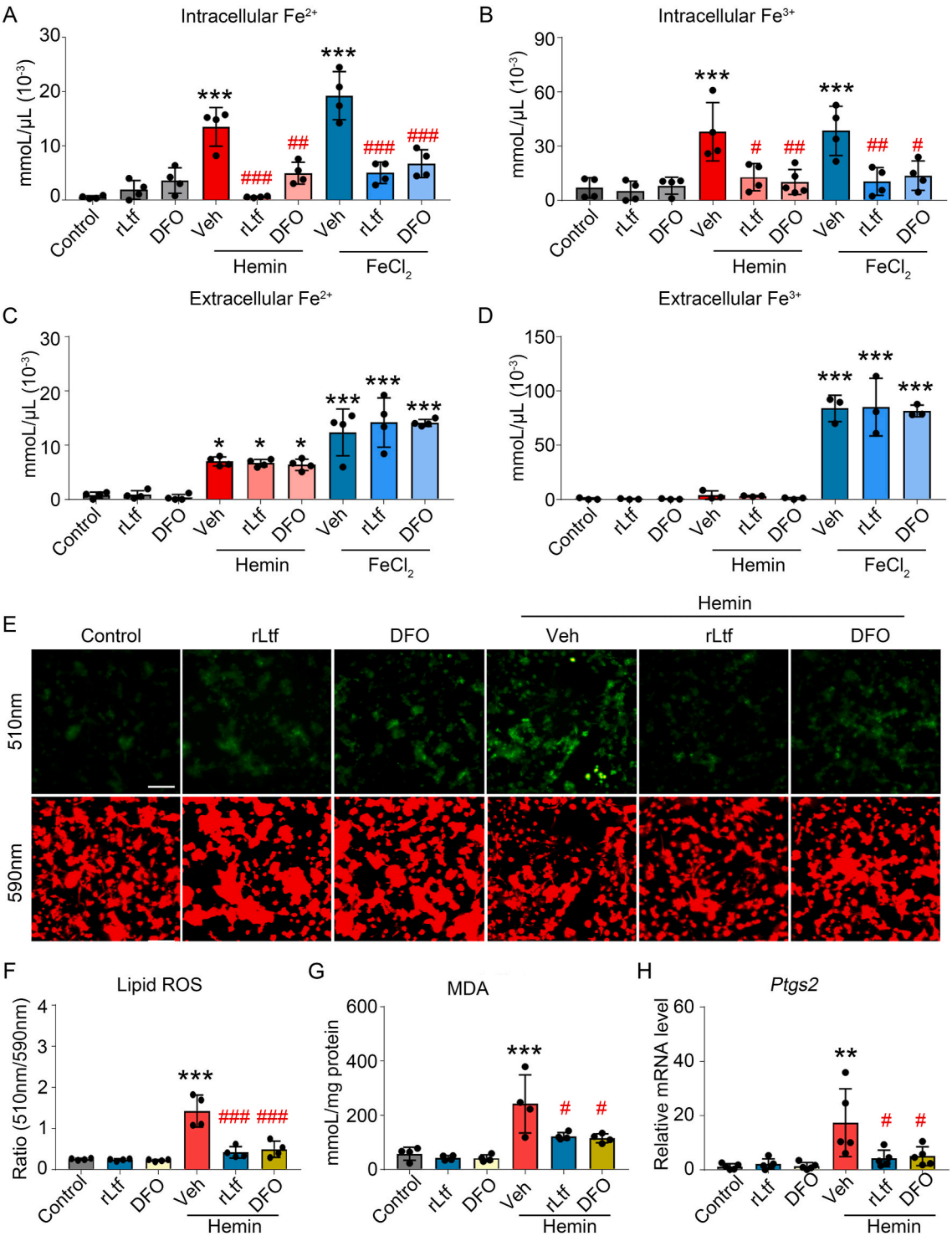

Fig. 5. Ltf rescues Hemin-induced ferroptosis by reducing intracellular iron concentrations in neurons. (A–D) Mouse primary neurons were treated as indicated for 4 h. The iron concentrations were measured by the Iron Assay Kit. The quantifications of intracellular Fe^{2+} (A) and Fe^{3+} (B) concentrations in neurons, and extracellular Fe^{2+} (C) and Fe^{3+} (D) concentrations in the medium are shown. **(E–H)** Mouse primary neurons were treated as indicated for 8 h. The lipid ROS were analyzed by fluorescence probe. The representative images (E) and quantifications (F) are shown. Malondialdehyde (MDA) content was measured using a commercial kit (G). The mRNA level of *Ptgs2* gene in primary neuron was detected by real-time RT-PCR (H), and *GAPDH* was served as the internal control. (A-D, F–H) One-way ANOVA followed Tukey's multiple comparisons test. *$p < 0.05$, **$p < 0.01$, ***$p < 0.001$ vs Control; #$p < 0.05$, ##$p < 0.01$, ###$p < 0.001$ vs corresponding Veh. Each experiment was repeated 4 (A-C, F, G), 3 (D), or 5 (H) times independently. Scale bar: (E) 100 μm.

observed that diabetic hyperglycemia increased neuronal ferroptosis in ipsilateral striatal neurons after ICH in mice. This is in keeping with our previous findings that poor outcomes of ICH were directly related to the severity of neuronal ferroptosis in the perihematomal region *in vivo* [6]. Interestingly, although hyperglycemia induces ferroptosis of osteoblast in type 2 diabetic osteoporosis [66], hyperglycemia was not the direct cause of neuronal ferroptosis, nor did it aggravate Hemin-induced neuronal ferroptosis. Therefore, neuronal ferroptosis aggravated by

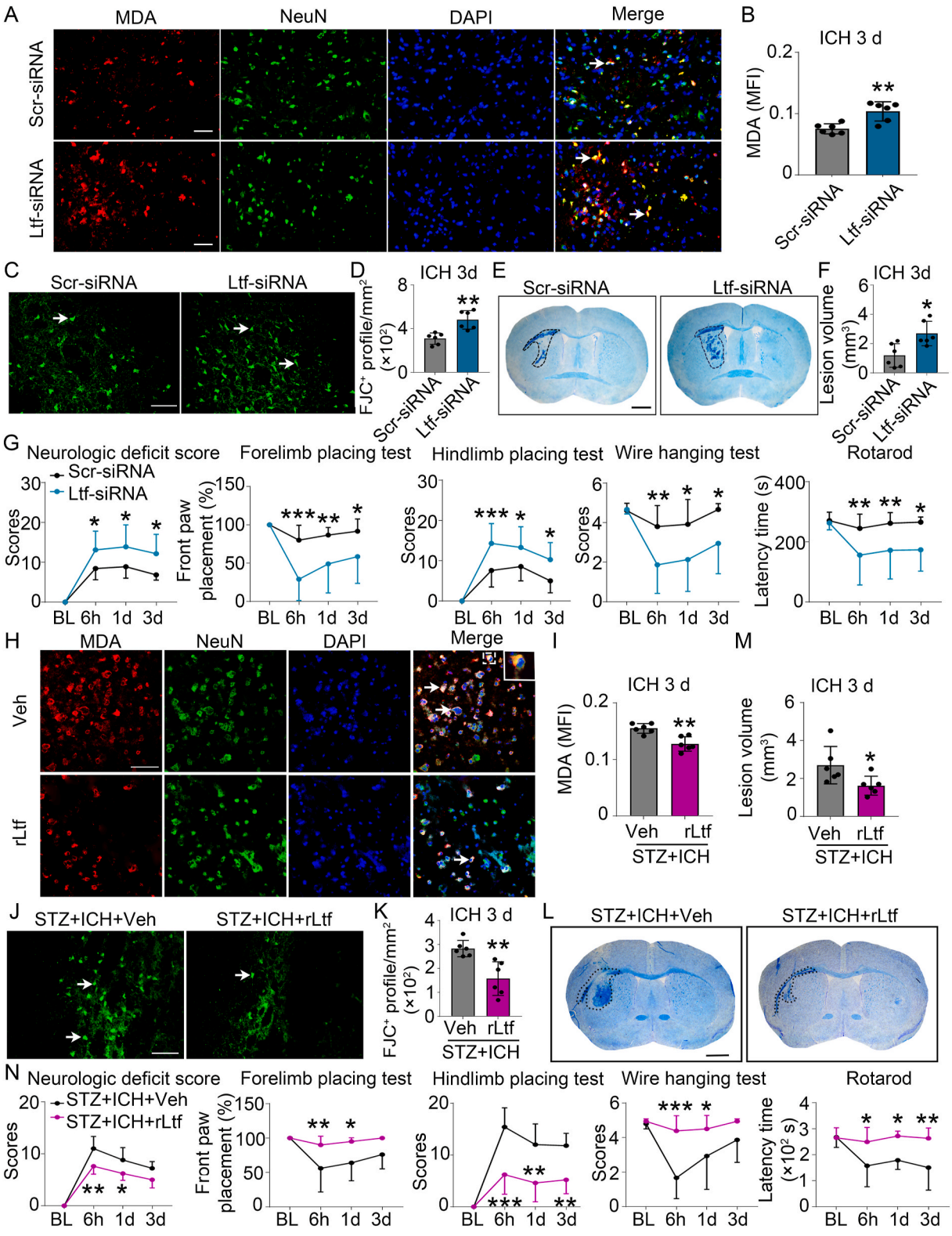

Fig. 6. Ltf rescues neuronal ferroptosis and improved acute outcomes in hyperglycemic ICH mice. (A–G) Ltf-siRNA or Scr-siRNA was injected intraventricularly to normoglycemic ICH mice. **(A, B)** Immunofluorescent staining using antibodies of MDA and NeuN. White arrows indicate the $MDA^{+}NeuN^{+}$ cells (A). The MFI of MDA was quantified (B). **(C, D)** FJC staining was performed and the FJC^{+} cells were quantified. White arrows indicate FJC^{+} cells. **(E, F)** CV/Luxol fast blue staining were performed to quantify the lesion volume (black dotted bordered). **(G)** Neurological function and motor function were examined following ICH blindly. **(H–N)** Four mg/kg of rLtf was administered (*i.p.*) to hyperglycemic ICH mice. Immunofluorescent staining using antibodies of MDA and NeuN (H, I), FJC staining (J, K), and CV/Luxol fast blue staining (L, M) were performed. The representative images (H, J, L) and quantifications (I, K, M) are shown. Neurological function and motor function were examined following ICH blindly (N). (B, D, F, I, K, M) Student's *t*-test followed by Welch's correction. (G, N) Two-way ANOVA followed by Tukey's multiple comparisons test. $^{*}p < 0.05$, $^{**}p < 0.01$, $^{***}p < 0.001$ vs corresponding Scr-siRNA (B, D, F, G) or corresponding Veh (I, K, M, N). Each group contained 6 (B, D, F, I, K, M) or 8 (G, N) animals. Scale bar: (A, H) 75 μm, (C, J) 50 μm, (E, L) 1 mm. Each experiment was repeated at least 3 times independently. (For interpretation of the references to color in this figure legend, the reader is referred to the Web version of this article.)

diabetic hyperglycemia after ICH was more likely to be influenced by other cells.

Neutrophils, on the other hand, are one of the most important peripheral cells in diabetes. Dysfunction of neutrophils has been considered as one of the main causes of impaired peripheral wound healing in diabetes [67]. However, it was unclear that whether peripheral neutrophils affect the central nerve system in conditions of hyperglycemic ICH. We found that peroxisome proliferator-activated receptor γ (PPARγ) transcribed *Ltf* in neutrophils, and the decreased expression/-secretion of neutrophilic Ltf in diabetic hyperglycemia was due to impaired PPAR-γ signaling pathway and can be reversed by adding PPAR-γ agonists rosiglitazone (ROSI). In line with our findings, ROSI is widely used in the treatment of type 2 diabetes in the clinic [68], and has been shown to reduce neurological dysfunction in ICH animal [69,70]. Thus, upregulating neutrophilic *Ltf* could be one of its beneficial therapeutic effects of activating PPARγ.

Although we are the first to discover the role of Ltf in rescuing neuronal ferroptosis after ICH, it has long been believed that Ltf plays important roles in the regulation of iron metabolism, immune regulation, antioxidation, anti-cancer, and anti-infection (including anti-COVID-19 virus infection [71]) and other aspects [25,72]. Although one study reported that silencing *Ltf* with shRNA or through upregulation of its E3 ligase NEDD4L deceased intracellular iron accumulation and subsequent ferroptosis in pancreatic cancer cells [73]. More recent research shows that apo-Ltf (an iron-free form of Ltf, which is used in our study) upregulated the expression of SLC7A11 (a subunit of cysteine/glutamate antiporter), and consequent in increasing glutathione (GSH) generation and inhibiting ferroptosis in breast cancer cells [74]. These data suggest the role of Ltf in ferroptosis is complicated: it may depend on iron saturation statues (apo or holo form) of Ltf, and it may also have cell-specificity. Importantly, Ltf accesses the blood bran barrier (BBB) via receptor-mediated transcytosis, because Ltf receptors are highly expressed on the surface of the brain endothelial cells [75,76]. Additionally, research shows that orally and intravenously administered recombinant human Ltf had similarities in the up-regulation of specific genes involved in oxidative stress and inflammatory responses for both routes of treatments [77]. These findings provide evidence of intraperitoneally administration of Ltf can cross the BBB and treat brain cells efficiently.

Our study had some limitations. First, we only used the STZ-injected type 1 diabetes mouse model, and only the acute impact of hyperglycemia was investigated. Since the distinctive pathophysiological changes induced by diabetes mellitus (DM) do not occur during the first 2 weeks after STZ injection, a long-term study is necessary to investigate the chronic consequences of DM on ICH injury in the future. Clinical study shows that the incidence of ICH is higher in type 1 diabetes than in patients with type 2 diabetes [4]. However, to investigate whether the decrease of neutrophilic Ltf is also the main cause of aggravated neuronal ferroptosis and neurologic impairment after ICH in mice with type 2 diabetes would also be interested. Second, since activated microglia also secret Ltf [78], we immunostained Ltf with microglia/macrophage marker Iba1 or neutrophil marker Ly6G and found that the majority Ltf^+ cells were $Ly6G^+$, and the majority $Ly6G^+$ neutrophils expressed Ltf in normoglycemic mice post-ICH (Fig. S6F). These data indicate that neutrophils are the main cell source of producing Ltf, but not $Iba1^+$ cells (since the Ltf^+Iba1^+ cells were located in the hematoma core and the morphology of these cells was round and branchless, these cells could be infiltrated macrophages). In the future, transgenic mouse strains with knocking out or knocking in *Ltf* in neutrophils should be used in the future to further distinguish the role of Ltf in neutrophils and microglia/macrophage. Finally, sex differences have also been reported in post-ICH injury [79], and estrogen is a vital mediator of brain protection in diabetic female mice [80]. Since the female mice have shown significant resistance to the diabetogenic effect of STZ, the impact of DM was studied only in male animals [81]. Whether neutrophilic Ltf protects against neuronal ferroptosis in female ICH mice should be investigated in other DM animal models, such as autoimmune or genetically induced models.

In conclusion, we found that diabetic hyperglycemia aggravated neuronal ferroptosis and neurologic deficits after ICH. The cause was hyperglycemia-impaired PPAR-γ activity in peripheral neutrophils and decreased the transcription of *Ltf*. Silencing *Ltf* in the ipsilateral brain aggravated neuronal ferroptosis and neurologic deficits, while administering recombinant Ltf inhibited neuronal loss and improved ICH outcomes *in vivo*. Additionally, neutrophilic Ltf rescued Hemin-induced neuronal ferroptosis by reducing intracellular iron concentration, and the lack of neutrophilic Ltf aggravated neuronal ferroptosis. These novel findings fill a gap in knowledge regarding the role of peripheral neutrophils in neuronal ferroptosis after ICH with diabetes and provide a vital foundation to develop neutrophil-based cell therapy or iron-binding protein-based therapy for treating ICH.

Author contributions

Designed experiments and finalized the manuscript: Zhongnan Xiao and Qian Li.

Performed experiments: Zhongnan Xiao, Danmin Shen, Ting Lan, Chao Wei, Qingyu Sun, Weihua Wu, Zhaoli Luo, Wen Chen, Yurui Zhang and Liye Hu.

Collected and analyzed data: Zhongnan Xiao, Danmin Shen, Ting Lan, Chao Wei, Qingyu Sun, Weihua Wu, Zhaoli Luo, Chenguang Zhang, Yamei Wang, Yabin Lu, Peipei Wang, Fei Yang and Qian Li.

Critical revision of the manuscript for important intellectual content: Qian Li and Fei Yang.

Funding

This work was supported by the National Natural Science Foundation of China (grant numbers 81873790, 32070735 and 81971037); The Beijing Natural Science Foundation Program and Scientific Research Key Program of Beijing Municipal Commission of Education (grant numbers KZ202010025033 and KZ201910025026); Support Project of High-level Teachers in Beijing Municipal Universities in the Period of 13th Five–year Plan (grant number CIT&TCD201904092).

Data and materials availability

All data are available in the main text or the supplementary materials.

Declaration of competing interest

The authors declare no potential conflicts of interest.

Appendix A. Supplementary data

Supplementary data to this article can be found online at https://doi.org/10.1016/j.redox.2022.102256.

References

[1] S.S. Virani, A. Alonso, E.J. Benjamin, et al., Heart disease and stroke statistics-2020 update: a report from the American heart association, Circulation 141 (9) (2020) e139–e596.
[2] C.S. Gray, J.F. Scott, J.M. French, K.G. Alberti, J.E. O'Connell, Prevalence and prediction of unrecognised diabetes mellitus and impaired glucose tolerance following acute stroke, Age Ageing 33 (1) (2004) 71–77.
[3] A. Saxena, C.S. Anderson, X. Wang, et al., Prognostic significance of hyperglycemia in acute intracerebral hemorrhage: the INTERACT2 study, Stroke 47 (3) (2016) 682–688.
[4] R. Liebkind, D. Gordin, D. Strbian, et al., Diabetes and intracerebral hemorrhage: baseline characteristics and mortality, Eur. J. Neurol. 25 (6) (2018) 825–832.
[5] J. Wan, H. Ren, J. Wang, Iron toxicity, lipid peroxidation and ferroptosis after intracerebral haemorrhage, Stroke Vasc Neurol 4 (2) (2019) 93–95.

[6] Q. Li, X. Han, X. Lan, et al., Inhibition of neuronal ferroptosis protects hemorrhagic brain, JCI Insight 2 (7) (2017), e90777.
[7] G. Dang, Y. Yang, G. Wu, Y. Hua, R.F. Keep, G. Xi, Early erythrolysis in the hematoma after experimental intracerebral hemorrhage, Transl. Stroke Res. 8 (2) (2017) 174–182.
[8] B.R. Stockwell, X. Jiang, W. Gu, Emerging mechanisms and disease relevance of ferroptosis, Trends Cell Biol. 30 (6) (2020) 478–490.
[9] S.J. Dixon, K.M. Lemberg, M.R. Lamprecht, et al., Ferroptosis: an iron-dependent form of nonapoptotic cell death, Cell 149 (5) (2012) 1060–1072.
[10] P. Dharmalingam, G. Talakatta, J. Mitra, et al., Pervasive genomic damage in experimental intracerebral hemorrhage: therapeutic potential of a mechanistic-based carbon nanoparticle, ACS Nano 14 (3) (2020) 2827–2846.
[11] I. Alim, J.T. Caulfield, Y. Chen, et al., Selenium drives a transcriptional adaptive Program to block ferroptosis and treat stroke, Cell 177 (5) (2019) 1262–1279.
[12] S. Chen, J. Peng, P. Sherchan, et al., TREM2 activation attenuates neuroinflammation and neuronal apoptosis via PI3K/Akt pathway after intracerebral hemorrhage in mice, J. Neuroinflammation 17 (1) (2020) 168.
[13] S.S. Karuppagounder, I. Alim, S.J. Khim, et al., Therapeutic targeting of oxygen-sensing prolyl hydroxylases abrogates ATF4-dependent neuronal death and improves outcomes after brain hemorrhage in several rodent models, Sci. Transl. Med. 8 (328) (2016) 328r–329r.
[14] Q. Li, A. Weiland, X. Chen, et al., Ultrastructural characteristics of neuronal death and white matter injury in mouse brain tissues after intracerebral hemorrhage: coexistence of ferroptosis, autophagy, and necrosis, Front. Neurol. 9 (2018) 581.
[15] S. Lattanzi, C. Cagnetti, L. Provinciali, M. Silvestrini, Neutrophil-to-Lymphocyte ratio predicts the outcome of acute intracerebral hemorrhage, Stroke 47 (6) (2016) 1654–1657.
[16] C. Tschoe, C.D. Bushnell, P.W. Duncan, M.A. Alexander-Miller, S.Q. Wolfe, Neuroinflammation after intracerebral hemorrhage and potential therapeutic targets, J STROKE 22 (1) (2020) 29–46.
[17] M.A. Cassatella, N.K. Ostberg, N. Tamassia, O. Soehnlein, Biological roles of neutrophil-derived granule proteins and cytokines, Trends Immunol. 40 (7) (2019) 648–664.
[18] J. Wang, S. Dore, Inflammation after intracerebral hemorrhage, J. Cerebr. Blood Flow Metabol. 27 (5) (2007) 894–908.
[19] J. Wang, Preclinical and clinical research on inflammation after intracerebral hemorrhage, Prog. Neurobiol. 92 (4) (2010) 463–477.
[20] C. Gong, J.T. Hoff, R.F. Keep, Acute inflammatory reaction following experimental intracerebral hemorrhage in rat, Brain Res. 871 (1) (2000) 57–65.
[21] X. Zhao, G. Sun, H. Zhang, et al., Polymorphonuclear neutrophil in brain parenchyma after experimental intracerebral hemorrhage, Transl. Stroke Res. 5 (5) (2014) 554–561.
[22] B. Wang, Y.P. Timilsena, E. Blanch, B. Adhikari, Lactoferrin: structure, function, denaturation and digestion, Crit. Rev. Food Sci. Nutr. 59 (4) (2019) 580–596.
[23] J.K. Actor, S.A. Hwang, M.L. Kruzel, Lactoferrin as a natural immune modulator, Curr. Pharmaceut. Des. 15 (17) (2009) 1956–1973.
[24] B. Lonnerdal, S. Iyer, Lactoferrin: molecular structure and biological function, Annu. Rev. Nutr. 15 (1995) 93–110.
[25] M.L. Kruzel, M. Zimecki, J.K. Actor, Lactoferrin in a context of inflammation-induced pathology, Front. Immunol. 8 (2017) 1438.
[26] P.A. Lapchak, J.H. Zhang, L.J. Noble-Haeusslein, RIGOR guidelines: escalating STAIR and STEPS for effective translational research, Transl. Stroke Res. 4 (3) (2013) 279–285.
[27] C.D. Chiu, C.C. Chen, C.C. Shen, et al., Hyperglycemia exacerbates intracerebral hemorrhage via the downregulation of aquaporin-4: temporal assessment with magnetic resonance imaging, Stroke 44 (6) (2013) 1682–1689.
[28] L. Wang, L. Kong, F. Wu, Y. Bai, R. Burton, Preventing chronic diseases in China, Lancet (N. Am. Ed.) 366 (9499) (2005) 1821–1824.
[29] H. Pu, Y. Shi, L. Zhang, et al., Protease-independent action of tissue plasminogen activator in brain plasticity and neurological recovery after ischemic stroke, Proc. Natl. Acad. Sci. U. S. A. 116 (18) (2019) 9115–9124.
[30] Q. Liu, E.M. Johnson, R.K. Lam, et al., Peripheral TREM1 responses to brain and intestinal immunogens amplify stroke severity, Nat. Immunol. 20 (8) (2019) 1023–1034.
[31] Q. Liu, N. Sanai, W.N. Jin, A. La Cava, L. Van Kaer, F.D. Shi, Neural stem cells sustain natural killer cells that dictate recovery from brain inflammation, Nat. Neurosci. 19 (2) (2016) 243–252.
[32] S.Q. Du, X.R. Wang, W. Zhu, et al., Acupuncture inhibits TXNIP-associated oxidative stress and inflammation to attenuate cognitive impairment in vascular dementia rats, CNS Neurosci. Ther. 24 (1) (2018) 39–46.
[33] H. Nakajima, T. Kubo, Y. Semi, et al., A rapid, targeted, neuron-selective, in vivo knockdown following a single intracerebroventricular injection of a novel chemically modified siRNA in the adult rat brain, J. Biotechnol. 157 (2) (2012) 326–333.
[34] H. Wu, T. Wu, W. Hua, et al., PGE2 receptor agonist misoprostol protects brain against intracerebral hemorrhage in mice, Neurobiol. Aging 36 (3) (2015) 1439–1450.
[35] H. Wu, T. Wu, X. Han, et al., Cerebroprotection by the neuronal PGE2 receptor EP2 after intracerebral hemorrhage in middle-aged mice, J. Cerebr. Blood Flow Metabol. 37 (1) (2017) 39–51.
[36] R.R. Ratan, The chemical biology of ferroptosis in the central nervous system, Cell Chem. Biol. 27 (5) (2020) 479–498.
[37] S.S. Karuppagounder, L. Alin, Y. Chen, et al., N-acetylcysteine targets 5 lipoxygenase-derived, toxic lipids and can synergize with prostaglandin E2 to inhibit ferroptosis and improve outcomes following hemorrhagic stroke in mice, Ann. Neurol. 84 (6) (2018) 854–872.
[38] M. Zille, S.S. Karuppagounder, Y. Chen, et al., Neuronal death after hemorrhagic stroke in vitro and in vivo shares features of ferroptosis and necroptosis, Stroke 48 (4) (2017) 1033–1043.
[39] H. Feng, K. Schorpp, J. Jin, et al., Transferrin receptor is a specific ferroptosis marker, Cell Rep. 30 (10) (2020) 3411–3423.
[40] B.R. Stockwell, A.J. Friedmann, H. Bayir, et al., Ferroptosis: a regulated cell death nexus linking metabolism, redox biology, and disease, Cell 171 (2) (2017) 273–285.
[41] M. Zille, S.S. Karuppagounder, Y. Chen, et al., Neuronal death after hemorrhagic stroke in vitro and in vivo shares features of ferroptosis and necroptosis, Stroke 48 (4) (2017) 1033–1043.
[42] L. Zhu, X. Chen, X. He, Y. Qi, Y. Yan, [Effect of exogenous hydrogen sulfide on BACE-1 enzyme expression and beta-amyloid peptide metabolism in high-glucose primary neuronal culture], Nan Fang Yi Ke Da Xue Xue Bao 34 (4) (2014) 504–506, 510.
[43] S. Wohnsland, H.F. Burgers, W. Kuschinsky, M.H. Maurer, Neurons and neuronal stem cells survive in glucose-free lactate and in high glucose cell culture medium during normoxia and anoxia, Neurochem. Res. 35 (10) (2010) 1635–1642.
[44] M. Xue, B.M. Del, Comparison of brain cell death and inflammatory reaction in three models of intracerebral hemorrhage in adult rats, J. Stroke Cerebrovasc. Dis. 12 (3) (2003) 152–159.
[45] G.S. Pinkus, J.L. Pinkus, Myeloperoxidase: a specific marker for myeloid cells in paraffin sections, Mod. Pathol. 4 (6) (1991) 733–741.
[46] J. Aronowski, C.E. Hall, New horizons for primary intracerebral hemorrhage treatment: experience from preclinical studies, Neurol. Res. 27 (3) (2005) 268–279.
[47] M. Li, Z. Li, Y. Yao, et al., Astrocyte-derived interleukin-15 exacerbates ischemic brain injury via propagation of cellular immunity, Proc. Natl. Acad. Sci. U. S. A. 114 (3) (2017) E396–E405.
[48] P. Presicce, C.W. Park, P. Senthamaraikannan, et al., IL-1 signaling mediates intrauterine inflammation and chorio-decidua neutrophil recruitment and activation, JCI Insight 3 (6) (2018).
[49] C.B. Crayne, S. Albeituni, K.E. Nichols, R.Q. Cron, The immunology of macrophage activation syndrome, Front. Immunol. 10 (2019) 119.
[50] M. Sielska, P. Przanowski, M. Pasierbinska, et al., Tumour-derived CSF2/granulocyte macrophage colony stimulating factor controls myeloid cell accumulation and progression of gliomas, Br. J. Cancer 123 (3) (2020) 438–448.
[51] A.D. Osafo-Addo, E.L. Herzog, CCL2 and T cells in pulmonary fibrosis: an old player gets a new role, Thorax 72 (11) (2017) 967–968.
[52] C. Sun, A. Wiestner, Under the microscope: CCL3 and T cells in the microenvironment of chronic lymphocytic leukemia, Leuk. Lymphoma 57 (3) (2016) 501–502.
[53] M. Guo, C. Li, Y. Lei, S. Xu, D. Zhao, X.Y. Lu, Role of the adipose PPARgamma-adiponectin axis in susceptibility to stress and depression/anxiety-related behaviors, Mol. Psychiatr. 22 (7) (2017) 1056–1068.
[54] J. Tomas, C. Mulet, A. Saffarian, et al., High-fat diet modifies the PPAR-gamma pathway leading to disruption of microbial and physiological ecosystem in murine small intestine, Proc. Natl. Acad. Sci. U. S. A. 113 (40) (2016) E5934–E5943.
[55] Q. Li, J. Wan, X. Lan, X. Han, Z. Wang, J. Wang, Neuroprotection of brain-permeable iron chelator VK-28 against intracerebral hemorrhage in mice, J. Cerebr. Blood Flow Metabol. 37 (9) (2017) 3110–3123.
[56] Y.J. Wang, Z.X. Li, H.Q. Gu, et al., China stroke statistics 2019: a report from the national center for healthcare quality management in neurological diseases, China national clinical research center for neurological diseases, the Chinese stroke association, national center for chronic and non-communicable disease control and prevention, Chinese center for disease control and prevention and institute for global neuroscience and stroke collaborations, Stroke Vasc Neurol 5 (3) (2020) 211–239.
[57] H. Irvine, S. Male, J. Robertson, C. Bell, O. Bentho, C. Streib, Reduced intracerebral hemorrhage and perihematomal edema volumes in diabetics on sulfonylureas, Stroke 50 (4) (2019) 995–998.
[58] X. Lin, Y. Tang, B. Sun, et al., Cerebral glucose metabolism: influence on perihematomal edema formation after intracerebral hemorrhage in cat models, Acta Radiol. 51 (5) (2010) 549–554.
[59] J. Liu, D. Wang, R. Yuan, Y. Xiong, M. Liu, Prognosis of 908 patients with intracerebral hemorrhage in Chengdu, Southwest of China, Int. J. Neurosci. 127 (7) (2017) 586–591.
[60] K. Mishiro, T. Imai, S. Sugitani, et al., Diabetes mellitus aggravates hemorrhagic transformation after ischemic stroke via mitochondrial defects leading to endothelial apoptosis, PLoS One 9 (8) (2014), e103818.
[61] J.P. Desilles, V. Syvannarath, V. Ollivier, et al., Exacerbation of thromboinflammation by hyperglycemia precipitates cerebral infarct growth and hemorrhagic transformation, Stroke 48 (7) (2017) 1932–1940.
[62] C.L. Baum, C.J. Arpey, Normal cutaneous wound healing: clinical correlation with cellular and molecular events, Dermatol. Surg. 31 (6) (2005) 674–686, 686.
[63] E. Hatanaka, P.T. Monteagudo, M.S. Marrocos, A. Campa, Neutrophils and monocytes as potentially important sources of proinflammatory cytokines in diabetes, Clin. Exp. Immunol. 146 (3) (2006) 443–447.
[64] J. Yang, Q. Li, Z. Wang, et al., Multimodality MRI assessment of grey and white matter injury and blood-brain barrier disruption after intracerebral haemorrhage in mice, Sci. Rep. 7 (2017) 40358.
[65] M.J. O'Donnell, S.L. Chin, S. Rangarajan, et al., Global and regional effects of potentially modifiable risk factors associated with acute stroke in 32 countries (INTERSTROKE): a case-control study, Lancet (N. Am. Ed.) 388 (10046) (2016) 761–775.

[66] H. Ma, X. Wang, W. Zhang, et al., Melatonin suppresses ferroptosis induced by high glucose via activation of the Nrf2/HO-1 signaling pathway in type 2 diabetic osteoporosis, Oxid. Med. Cell. Longev. 2020 (2020) 9067610.
[67] S.L. Wong, M. Demers, K. Martinod, et al., Diabetes primes neutrophils to undergo NETosis, which impairs wound healing, Nat. Med. 21 (7) (2015) 815–819.
[68] R.E. Soccio, E.R. Chen, M.A. Lazar, Thiazolidinediones and the promise of insulin sensitization in type 2 diabetes, Cell Metab. 20 (4) (2014) 573–591.
[69] X. Zhao, Y. Zhang, R. Strong, J.C. Grotta, J. Aronowski, 15d-Prostaglandin J2 activates peroxisome proliferator-activated receptor-gamma, promotes expression of catalase, and reduces inflammation, behavioral dysfunction, and neuronal loss after intracerebral hemorrhage in rats, J. Cerebr. Blood Flow Metabol. 26 (6) (2006) 811–820.
[70] X. Zhao, G. Sun, J. Zhang, et al., Hematoma resolution as a target for intracerebral hemorrhage treatment: role for peroxisome proliferator-activated receptor gamma in microglia/macrophages, Ann. Neurol. 61 (4) (2007) 352–362.
[71] C. Salaris, M. Scarpa, M. Elli, et al., Protective effects of lactoferrin against SARS-CoV-2 infection in vitro, Nutrients 13 (2) (2021).
[72] L. Moreno-Exposito, R. Illescas-Montes, L. Melguizo-Rodriguez, C. Ruiz, J. Ramos-Torrecillas, E. de Luna-Bertos, Multifunctional capacity and therapeutic potential of lactoferrin, Life Sci. 195 (2018) 61–64.
[73] Y. Wang, Y. Liu, J. Liu, R. Kang, D. Tang, NEDD4L-mediated LTF protein degradation limits ferroptosis, Biochem. Biophys. Res. Commun. 531 (4) (2020) 581–587.
[74] Z. Zhang, M. Lu, C. Chen, et al., Holo-lactoferrin: the link between ferroptosis and radiotherapy in triple-negative breast cancer, Theranostics 11 (7) (2021) 3167–3182.
[75] S. Sabra, M.M. Agwa, Lactoferrin, a unique molecule with diverse therapeutical and nanotechnological applications, Int. J. Biol. Macromol. 164 (2020) 1046–1060.
[76] C. Fillebeen, L. Descamps, M.P. Dehouck, et al., Receptor-mediated transcytosis of lactoferrin through the blood-brain barrier, J. Biol. Chem. 274 (11) (1999) 7011–7017.
[77] X. Zhao, M. Kruzel, J. Aronowski, Lactoferrin and hematoma detoxification after intracerebral hemorrhage, Biochem. Cell. Biol. 99 (1) (2021) 97–101.
[78] H. Xu, Y. Wang, N. Song, J. Wang, H. Jiang, J. Xie, New progress on the role of glia in iron metabolism and iron-induced degeneration of dopamine neurons in Parkinson's disease, Front. Mol. Neurosci. 10 (2017) 455.
[79] Y. Xie, Y.J. Li, B. Lei, et al., Sex differences in gene and protein expression after intracerebral hemorrhage in mice, Transl. Stroke Res. 10 (2) (2019) 231–239.
[80] A. Sakata, M. Mogi, J. Iwanami, et al., Female type 2 diabetes mellitus mice exhibit severe ischemic brain damage, J. Am. Soc. Hypertens. 5 (1) (2011) 7–11.
[81] H. Kolb, Mouse models of insulin dependent diabetes: low-dose streptozocin-induced diabetes and nonobese diabetic (NOD) mice, Diabetes Metab. Rev. 3 (3) (1987) 751–778.